

## Stress-driven infill mapping for 3D-printed continuous fiber composite with tunable infill density and morphology

Tong Liu<sup>a</sup>, Shangqin Yuan<sup>a,b,c,\*</sup>, Yaohui Wang<sup>d</sup>, Yi Xiong<sup>d</sup>, Jihong Zhu<sup>b,c</sup>, Lu Lu<sup>a,b</sup>, Yunlong Tang<sup>e,f,<sup>\*\*</sup></sup>

<sup>a</sup> Unmanned System Research Institute, Northwestern Polytechnical University, Xi'an, Shaanxi 710072, China

<sup>b</sup> State IJR Center of Aerospace Design and Additive Manufacturing, School of Mechanical Engineering, MIIT China, Northwestern Polytechnical University, Xi'an, Shaanxi 710072, China

<sup>c</sup> Key Laboratory of Metal High Performance Additive Manufacturing and Innovative Design, NPU-QMUL Joint Research Institute, Northwestern Polytechnical University, Xi'an, Shaanxi 710072, China

<sup>d</sup> School of System Design and Intelligent Manufacturing, Southern University of Science and Technology, Shenzhen 518055, China

<sup>e</sup> Mechanical and Aerospace Engineering Department Monash University, Melbourne 3800, Australia

<sup>f</sup> Materials Science and Engineering Department Monash University, Melbourne 3800, Australia



### ARTICLE INFO

**Keywords:**  
Continuous fiber composite via additive manufacturing  
Path planning  
Stress-driven design  
3D printing of composite

### ABSTRACT

Continuous fiber composite via additive manufacturing is an emerging field that extends the design freedom of composite structure as well as integrates with the digital fabrication approach. The path planning for continuous fiber is highly freedom to achieve tunable and desirable lightweight performance. Herein, a wave projection function is proposed to design the infill morphology and control the infill ratio corresponding to a specific vector field. The infill ratio and path orientation are simultaneously mapped with mechanical stress field distribution. The path planning algorithm via solving the traveling salesman problem (TSP) is employed to generate continuous fiber trajectories with minimized cutting points. As fabricated composite structure shows outstanding performance over these with conventional Zig-Zag infill pattern, which possesses identical infill ratio. The proposed infill approach can integrate with the topology optimized structure to concurrently optimize the infill fiber path and structural configuration. This generative design for composite structure is a typical AM-driven approach, which exhibits strong advantages to create adaptive infill patterns with complex geometry.

### 1. Introduction

Polymeric composites via additive manufacturing (AM) usually possess advantageous mechanical enhancement and multi-functional properties, which are obtained by engineering material distribution with composite structures from micro to macro-scales [1]. Continuous carbon fiber-reinforced polymer composites (CFRP) exhibit outstanding mechanical performance such as excellent specific strength and stiffness [2–4]. Continuous fiber composite via AM offers unique advantages to explore the design and manufacturing freedom of fiber orientation/volume ratio and part geometric complexity [5,6].

The conventional processes such as autoclave, automated fiber/tape placement (AFP/ATP) and resin transfer molding (RTM) usually fabricate the structure through laminating of fiber sheets and taps with the

help of a pre-fabricated mold, and then cure the polymer resin within the mold in a heated oven [7–10]. Thus, the geometry complexity and structure design freedom are strongly limited. Meanwhile, the fabrication processes of composite structures with hollow or lattice designs are quite complicated, and its process includes the steps of molding, mounting, etching and post-cleaning [11]. Therefore, manufacturing with lattice and hollow composite structures is time-consuming and expensive [12]. As compared with conventional composite manufacturing processes, AM techniques as free-form fabrication processes offer design and manufacturing freedom as well as eliminate the need for molds, tooling and save raw materials [13]. Thus, AM for composite is highly possible to open a new avenue for design and manufacture to utilize the anisotropic property of continuous fiber and achieve the spatial arrangement of fiber path within composite matrix

\* Corresponding author at: Unmanned System Research Institute, Northwestern Polytechnical University, Xi'an, Shaanxi 710072, China.

\*\* Corresponding author at: Mechanical and Aerospace Engineering Department Monash University, Melbourne 3800, Australia.

E-mail addresses: [shangqin.yuan@nwpu.edu.cn](mailto:shangqin.yuan@nwpu.edu.cn) (S. Yuan), [yunlong.tang1@monash.edu](mailto:yunlong.tang1@monash.edu) (Y. Tang).

[14].

With the advances in AM technologies, especially for CFRP structures, the mechanical and functional properties of composite structures attract intensive attention due to these structures being available to meet the stringent requirements for end-use applications [15,16]. Therefore, performance-driven design becomes an emerging research field to develop structural composite with lightweight and advanced functional performance [17,18,59]. The lightweight design for CFRP needs to fully explore the potential of fiber arrangement in spatial by AM

technique [19]. The engineerable fiber volume ratio and three-dimensional fiber orientation achieve structural optimization with proper fiber path planning, which is impossible to manufacture by molding or sheet lamination process [20,21].

The process-planning strategy for composite structures is critical to realize the performance-driven design from microfiber properties and structural topology in 3D [22]. To date, the modified fused deposition modeling (FDM) with in-situ impregnation is a simple AM process to fabricate continuous carbon fiber reinforced composite with a digitally

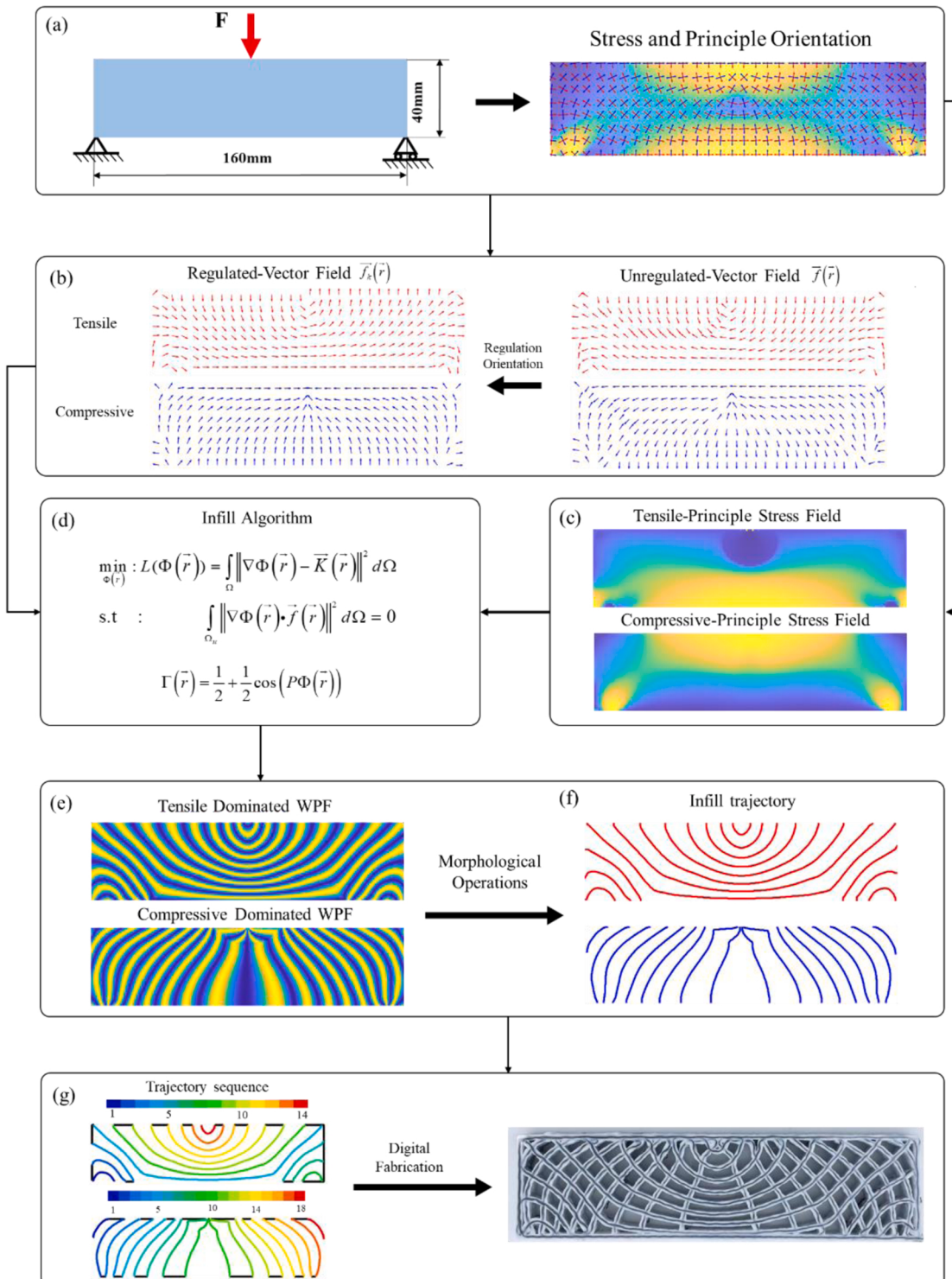


Fig. 1. Schematic diagram of structural design and fabrication process.

programmed toolpath for fiber arrangement [23,24]. Proper toolpath planning for 3D mode usually involve slicing and infill planning as well as process parameter mapped with toolpath [25–27]. Apart from the proper slicing algorithm, the unique design of infill morphology for the in-plane toolpath can be created to respond to external loads [28]. Here, the design of fiber orientation in mesoscale and structural configuration design in macroscale are both significant for performance-driven path design.

The in-plane toolpath via infill planning needs to generate the contour lines and infill lines to ensure the geometric design which is constructed by pre-programmed fiber/matrix distribution [29]. Duigou et al. reported that the change of layer thickness by the slicing program could tailor the mechanical properties due to its varied fiber volume ratio in each layer [30]. Moreover, other researches focus on contour and infill planning for in-plane fiber pattern. Matsuzaki et al. proposed a novel strategy of infill planning of continuous fiber through which CFRP with customized stiffness is developed by varying the localized volume ratio of continuous fibers [29]. Pedersen et al. reported that the orthotropic composites possess optimal mechanical properties by aligning with the direction of the principal stress [31,32]. Li et al. developed different path planning approaches to infill the engineering components with holes and topologized structures. It is worth noting that AM process can be well implemented to fabricate the CFRP with a conformal fiber path with different structure contours [33]. However, it is lacking parametric design strategy of infill line to digitally tune infill ratio as well as fiber fraction of composite structure via AM.

Recently, a stiffness-dominated optimization framework for structural topology incorporated with anisotropic composite is proposed. Wang et al. proposed a stress-vector tracing algorithm to integrate with the topological optimization method via solid orthotropic material with penalization (SOMP) in order to create a load-dependent path of continuous fiber [34]. Tehrani et al. reported that SOMP and level-set approaches of structural topology could further integrate with

morphology methods such as streamline, offset and equally-spaced methods, and these two-step sequential optimizations in 2D are feasible to generate continuous fiber paths for AM composite fabrication with desirable configurations [14,35]. These toolpath planning approaches mainly achieved compact infill lines to construct the topologized structures, and a single vector field is applied to guide the fiber alignment and orientation. However, these are not suitable for periodic or non-periodic infill path planning, which is usually with a hollow pattern or lattice design. Besides, it is challenging to map the concurrently optimal design of microscale material property and macroscale structural topology [36]. Therefore, an adaptive design strategy for infill mapping is necessary to be developed with conformal and tunable morphology and density.

Several manufacturing constraints need to be considered in the toolpath planning. Transverse isotropic strengthening is advantageous property of continuous fiber bundles, which is favorable to align with the principal stress orientation [37,38]. As compared with conventional FDM infill patterns, the infill patterns for continuous fibers need to satisfy the requirement of performance-enhancing as well as conformal infill [39].

Meanwhile, the manufacturable continuity regulation algorithm of the fiber path is necessary to adapt the microscale unit-cell or discrete orientation optimization model for fiber-reinforced structures. Groen et al. proposed a method to obtain manufacturable projected designs based on the solution of homogenization-based topology optimization (TO) on a coarse scale [40]. This high-resolution approach was identical to the conventional TO on the aspect of performances with more calculating efficiency and later extend for coated structures and truss design [41,42]. However, this approach cannot efficiently take advantages of fibers which cannot strictly aligned with principle stress direction in those high stress region due to the least square approach is used. More importantly, the specific process constraints such as filament spacing and volume fraction of carbon fiber are also not considered in

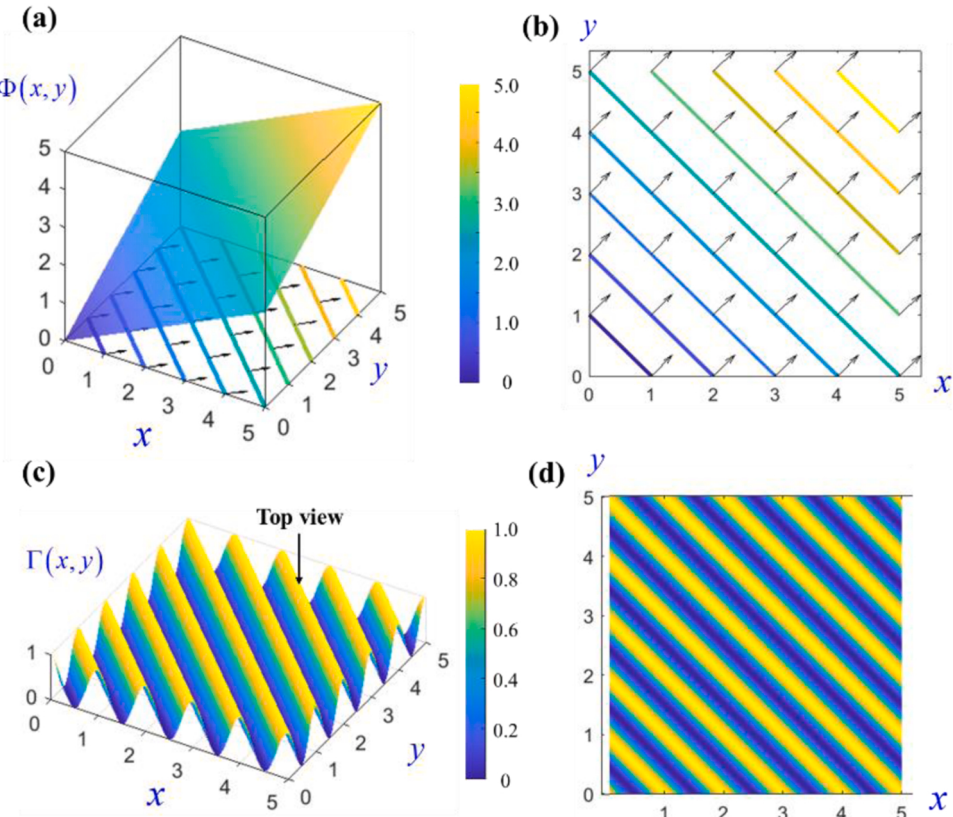


**Fig. 2.** (a) The phase function  $\Phi(x,y)$ ; (b) the isoline and the gradient of the phase function  $\Phi(x,y)$ ; (c) and (b) The wave function  $\Gamma(x,y)$ .

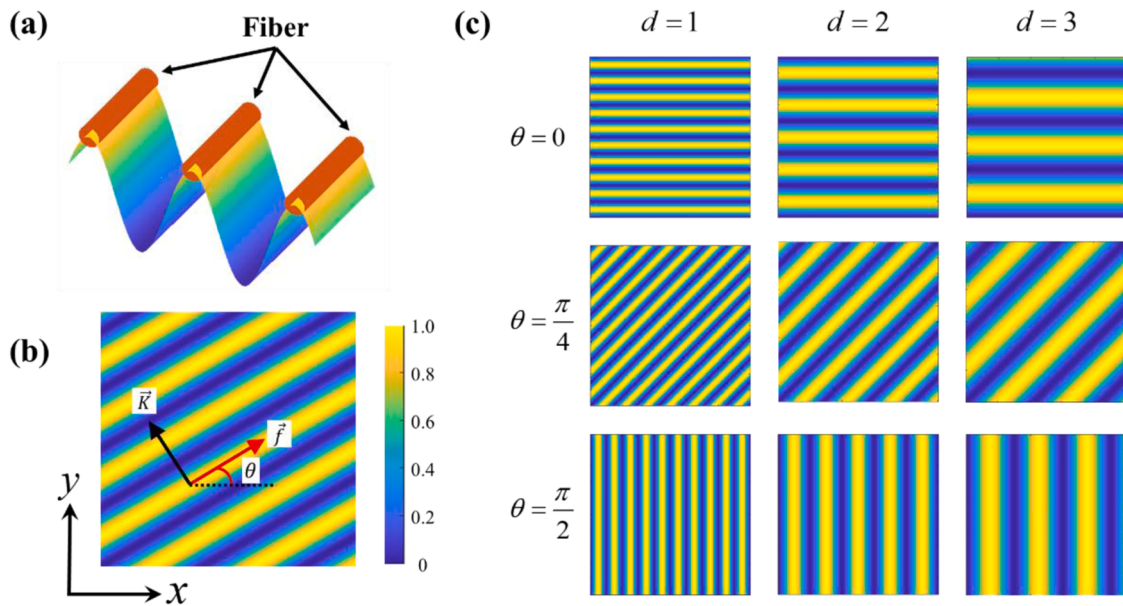


**Fig. 3.** (a) The schematic diagram of wave projection function and peak region representing fibers (b) illustration of propagation direction  $\vec{K}$ , fiber direction  $\vec{f}$  and fiber angle  $\theta$ ; (c) WPF 2D diagrams with different  $\theta$  and  $d$ .

the existing methods but show important role slicing and toolpath planning [43–45]. In order to realize the designed 2D or 3D patterns of CFRP composite, the processing planning also need to include the combinations of process parameters to fit with the planned fiber path and morphology with different curvature and spacing.

In this work, a stress field-based toolpath planning approach is proposed and coupled with a wave projection function (WPF) to generate continuous fiber trajectories and achieve an infill mapping. Specifically, the previously developed projection method [40] has been used and modified with a stress-based penalty term to ensure the fiber can strictly conform to the principle stress direction in high stress regions. During the developed projection process, the specific process constraints for fiber reinforced printing such as path spacing have been considered in the new developed process. This new approach can achieve parametric control by tuning the spacing factor to simultaneously monitor the infill density and morphology. To ensure the path continuity, cutting point minimization approach is developed by solving the defined Travelling Salesman Problem (TSP) problem. Ultimately, the infill pattern is the streamline extracted from the wave projection function mapped with the manufacturing process to infill the entire structure to achieve excellent lightweight performance. In summary, the major innovation of this paper can be summarized as:

- Develop a stress-based penalty term that can enable the fiber path can strictly follow the principle stress direction on the high stress regions;
- The specific process constraints for fiber reinforced printing such as path spacing have been considered in the developed process which enables the designed path is manufacturable;
- Process parameters mapping and printing path sequence optimization have been integrated in the proposed method. It supports the efficient and high quality printing of continuous fiber reinforced materials.

## 2. Methodology

This stress field-based infill approach aims to simultaneously control the fiber orientation and the infill ratio is tunable based on the stress distribution under given external loading. The local fiber orientation is employed to align with the local stress principal direction, which is a heuristic strategy that can enhance the mechanical performance of AM-fabricated structures for orthotropic materials. Under a given load condition, the principal stress field can be extracted through the finite element method (FEM) and the corresponding principal stress direction can be employed to control the fiber direction. A cosine wave is

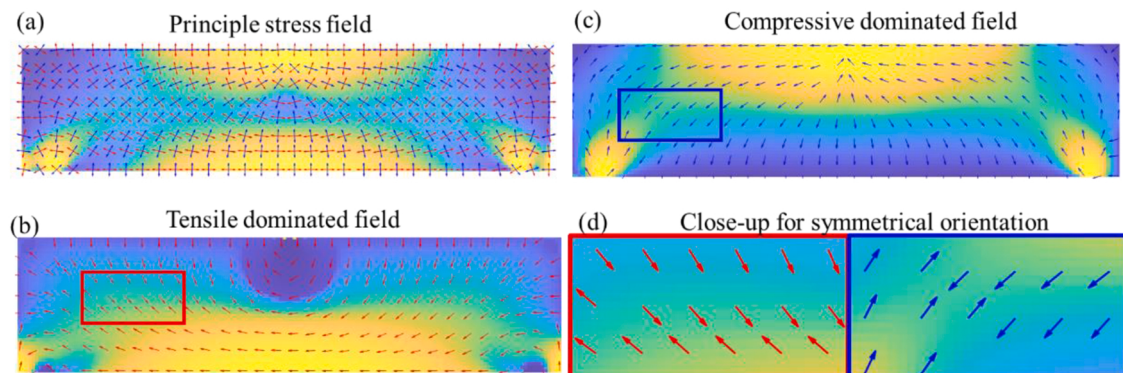


**Fig. 4.** Tensile and compressive dominated stress field and its orientation are extracted from the FEA quadrilateral mesh; (a) the stress field of each element under specific loading conditions; (b) the tensile stress field and its orientation; (c) the compressive stress field and its orientation; (d) zoom-out for turbulent orientation field.

introduced to build the relationship between the direction field and scalar field and represent the fiber trajectory. The direction of periodic wave propagation is perpendicular to the vibration direction. Fiber bundles will be aligned along with the peak reign of the cosine wave, and wavelength indicates the inter-fiber distance. Thus the local and global periodicity of the wave function can be applied to control fiber spacing and infill density respectively. The wave projection approach is a novel method to link the stress field with infill density and morphology. The tensile and compressive layers are printed alternatively, which shows the inherent advantage of composite laminates and fully exploits the design capability of toolpath planning in AM. The lightweight potential induced by composite material and structural design are well explored in such AM-enabled composite structures.

As shown in Fig. 1, the stress field based on the FEM can be decomposed into two stress fields including tensile-dominated and compressive-dominated ones. These stress fields are separately mapped with layers of infill patterns using the wave projection function (WPF). The local fiber spacing and fiber orientation are corresponding to the stress intensity and direction respectively. The individual fiber trajectory can be extracted from the peak of the WPF indicating fiber location. The sequence of infill paths is modeled as a TSP problem to minimize fiber cutting and can be solved by existing solvers. Finally, the digital code of toolpath planning is generated to realize the layer-by-layer fabrication process.

## 2.1. Stress field evaluation and principal stress extraction

The principal stress and direction of each element can be calculated from the stress tensor matrix  $\sigma$ :

$$\sigma = \begin{bmatrix} \sigma_{xx} & \tau_{xy} \\ \text{sym} & \sigma_{yy} \end{bmatrix} \quad (1)$$

$$(\sigma E - \sigma) \vec{f} = 0 \quad (2)$$

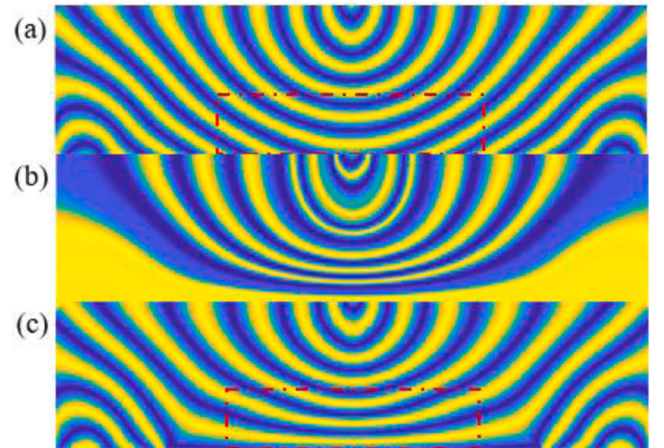


**Fig. 6.** (a) Unconstrained least squares results (b) Global Constrained Least Squares (c) Least Squares with Weight Constraints.

where  $\sigma_1, \sigma_2$  and  $\vec{f}_1, \vec{f}_2$  are obtained by solving the eigenvalues and eigenvectors of Eq. (2).  $\sigma_1, \sigma_2$  are corresponding to the tensile and compressive value of principal stress respectively.  $\vec{f}_1, \vec{f}_2$  are corresponding to the tensile and compressive direction of principal stress respectively [46].  $\sigma_1, \sigma_2$  and  $\vec{f}_1, \vec{f}_2$  is a spatially varied value, therefore, for any point P in design space  $\Omega$ , it can be reformed as  $\sigma_1(\vec{r}), \sigma_2(\vec{r})$  and  $\vec{f}_1(\vec{r}), \vec{f}_2(\vec{r})$ , where  $\vec{r}$  is the position vector of point P.  $\vec{f}_1(\vec{r}), \vec{f}_2(\vec{r})$  is the direction vector which can also be rewritten as

$$\vec{f}(\vec{r}) = [\cos \theta(\vec{r}) \quad \sin \theta(\vec{r})]^T \quad (3)$$

wherein  $\theta(\vec{r})$  is the direction angle of  $\vec{f}(\vec{r})$ . Parameters  $\sigma_1(\vec{r}), \sigma_2(\vec{r})$ ,

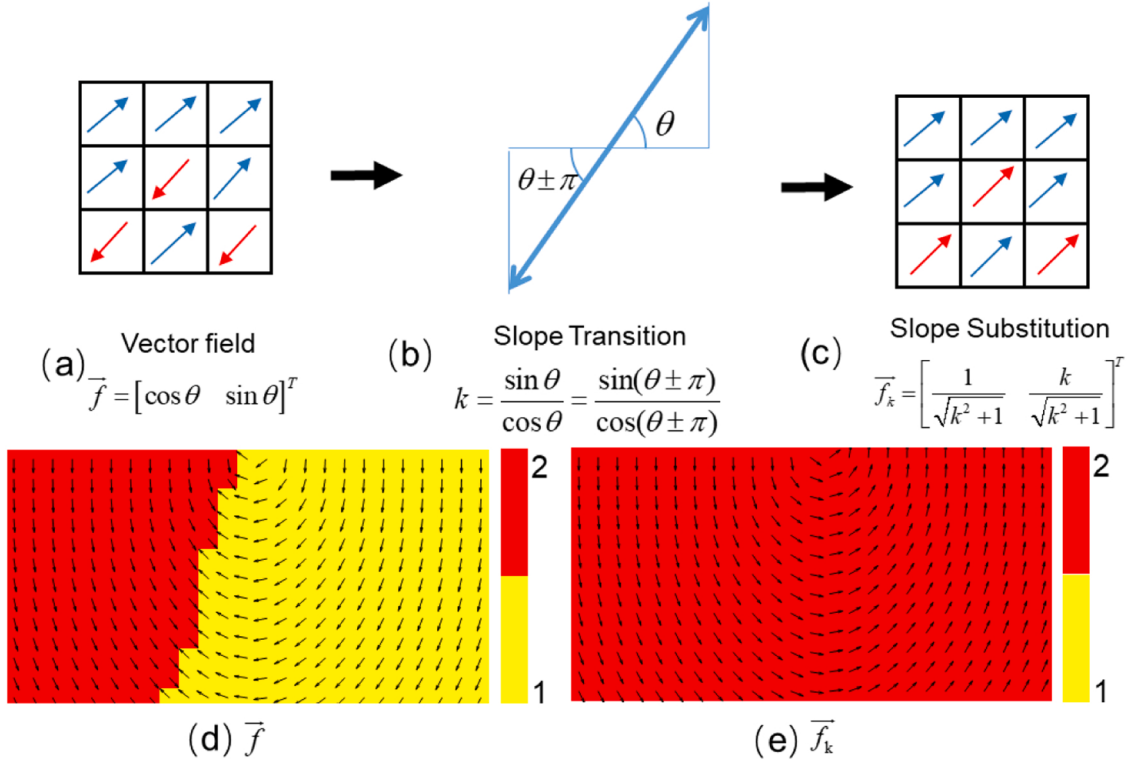


**Fig. 5.** (a) The raw and turbulent vector field of  $\vec{f}$  is extracted from finite element analysis and (b) slope substitution orientation regulation method, (c) the regulated field of  $\vec{f}_k$  is obtained by rotational transformation, (d) unregulated vector field, (e) regulated vector field.

$f_1(\vec{r})$  and  $f_2(\vec{r})$  will be used to generate WPF, and the detail is shown in Section 2.4.

## 2.2. The wave projection function method

The wave projection method is proposed to build the relationship between the vector field and the phase field (or scalar field) so that it can map the vector field. The synthesis algorithm proposed by Rumpf et al. [47] reveals the relationship between the phase field function  $\Phi(\vec{r})$  and the vector field  $\vec{K}(\vec{r})$ . For example, a phase field function  $\Phi(\vec{r})$  can be expressed by the following equation:

$$\Phi(\vec{r}) = \vec{K}(\vec{r}) \cdot \vec{r} \quad (4)$$

where the  $\vec{K}(\vec{r})$  is the vector field and  $\vec{r}$  is the position vector.

Let  $\vec{r} = [x \ y]^T$  and  $\vec{K}(\vec{r}) = \vec{K}(x, y) = [\frac{1}{2} \ \frac{1}{2}]^T$ , then combining Eq. (4),  $\Phi(\vec{r}) = \Phi(x, y) = \frac{1}{2}(x + y)$ ; As shown in Fig. 2(a), the vector field  $\vec{K}(\vec{r})$  is the gradient of the phase function  $\Phi(x, y)$ , and it is perpendicular to the isoline of the phase function  $\Phi(x, y)$ ; Substituting the phase field function  $\Phi(x, y)$  into the wave function  $\Gamma(x, y)$ . It can be derived as follows:

$$\Gamma(x, y) = \frac{1}{2} + \frac{1}{2} \cos(2\pi\Phi(x, y)) \quad (5)$$

As shown in Fig. 2(c), the peak region of the cosine function  $\Gamma(x, y)$  is consistent with the distribution of the isoline of the phase function  $\Phi(x, y)$ , and the distribution of the peak region of  $\Gamma(\vec{r})$  can project the vector field  $\vec{K}(\vec{r})$ . Moreover, as mentioned above, the cosine function is used as the infill pattern to represent fibers (Fig. 3(a)). To obtain the infill pattern mapping with principal stress distribution within a design domain, the wave projection function (WPF)  $\Gamma(\vec{r})$  is introduced as follows:

$$\Gamma(\vec{r}) = \frac{1}{2} + \frac{1}{2} \cos(P\vec{K}(\vec{r}) \cdot \vec{r}) \quad (6)$$

where  $\vec{K}(\vec{r})$  is the propagation direction which is perpendicular to the

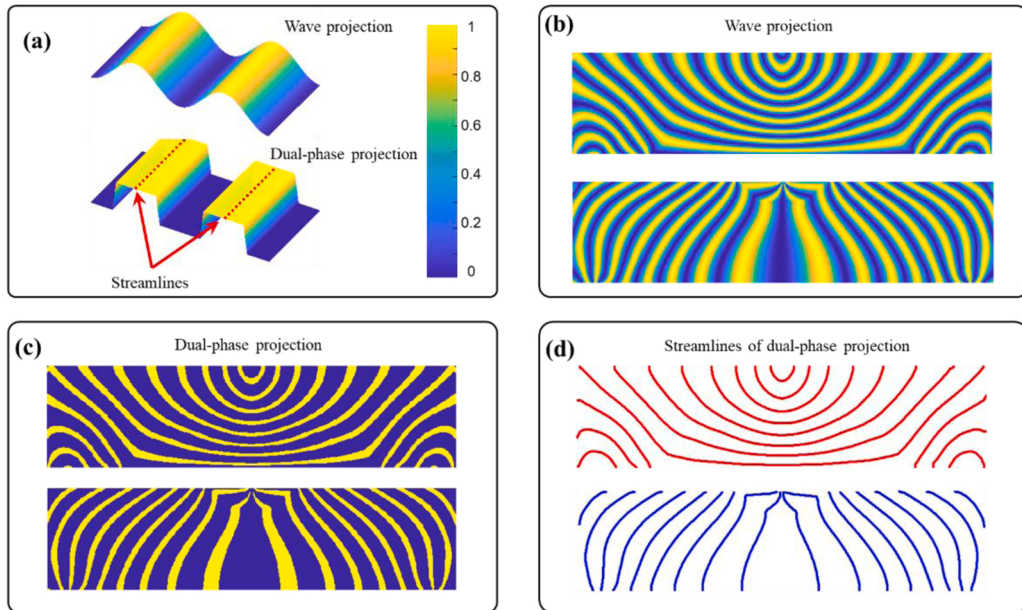


**Fig. 7.** (a) Schematic of the wave projection and streamlines of dual-phase projection; (b) Tensile and Compressive stress dominated wave projection  $\Gamma_1(\vec{r})$  and  $\Gamma_2(\vec{r})$ ; (c) Tensile and Compressive stress dominated dual-phase projection  $\Gamma_{11}(\vec{r})$  and  $\Gamma_{12}(\vec{r})$ ; (d) Tensile and Compressive stress dominated streamline  $I_1(\psi)$  and  $I_2(\psi)$ .

fiber direction  $\vec{f}(\vec{r})$  (shown in Fig. 3(b)), it is defined as:

$$\vec{K}(\vec{r}) = [-\sin \theta \ \cos \theta]^T \quad (7)$$

$P$  is defined as

$$P = \frac{2\pi}{d} \quad (8)$$

where  $d$  is the spacing factor (SF). The WPF with different  $\theta$  and  $d$  is shown in Fig. 3(c).

## 2.3. Orientation regulation

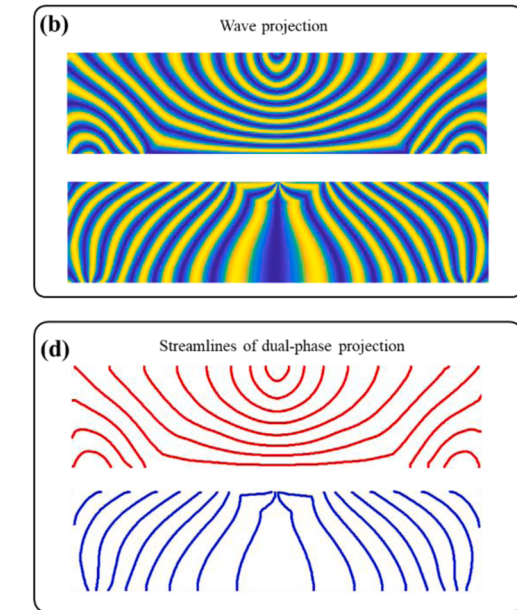
Since the principal stress directions indicated by  $\theta$  are rotationally symmetric (shown in Fig. 4(b) and (c)), the turbulent vector field will disorder the WPF  $\Gamma(\vec{r})$ . This is due to the periodicity of the tangent function causing the jump  $\pi$  of the angle in the process of obtaining the angle by the arc-tangent and then extracting major or minor stress vectors that are inverse but symmetric. The locally labeled vector usually flips inversely. Chen et al. [48] proposed a minimal spanning tree (MST) approach and Groen et al. [40] suggested an image processing approach called connected component labeling to achieve a smoothly varying angle field  $\theta$ . In order to simplify the calculation, a rotational transformation of singularity elimination is proposed, and it is applied by slope justification of each element. Orientation regulation(OR) is proposed to re-oriented the angle  $\theta$  by  $\pi$ , which will not influence the mechanical performance of resulted structures. The orientation regulation by local slope justification is expressed below to convert the inconsistent angle field. For such the case, the value of the angle  $\theta$  changes and it satisfies:

$$\vec{f} = \begin{bmatrix} \cos \theta \\ \sin \theta \end{bmatrix} = - \begin{bmatrix} \cos(\theta \pm \pi) \\ \sin(\theta \pm \pi) \end{bmatrix} \quad (9)$$

The slope ratio of each element is described as

$$k = \frac{\sin \theta}{\cos \theta} = \frac{\sin(\theta \pm \pi)}{\cos(\theta \pm \pi)} \quad (10)$$

The vector field regulation of  $\vec{f}$  and  $\vec{K}$  is conducted by a re-



orientation filter and substituted by the following  $\vec{f}_k$  and  $\vec{K}_k$ :

$$\vec{f}_k = \begin{bmatrix} \frac{1}{\sqrt{k^2 + 1}} \\ \frac{k}{\sqrt{k^2 + 1}} \end{bmatrix} \quad (11)$$

$$\vec{K}_k = \begin{bmatrix} -k \\ \frac{1}{\sqrt{k^2 + 1}} \end{bmatrix} \quad (12)$$

where  $\vec{f}_k$  indicates the newly regulated vector field of stress and  $\vec{K}_k$  is perpendicular to the stress vector  $\vec{f}_k$  in each element. As a result,  $\vec{f}_k$  are shown as smoothly varying angle field, which is available for further projection manipulation, the effect is as shown in Fig. 5(d) and (e).

#### 2.4. The WPF generation for spatially-variant-vector field

To obtain the infill pattern which can conform to the distribution of the given principal stress direction inside a design domain, the WPF  $\Gamma(\vec{r})$  shall be constructed. However, Eq. (6) cannot be applied directly when the propagation direction  $\vec{K}$  is spatially variant  $\vec{K}(\vec{r})$ . Therefore, a mapping function  $\Phi(\vec{r})$  needs to be established to match the spatial variable  $\vec{K}(\vec{r})$  [47]. The relation between the wave propagation vector  $\vec{K}$  and phase function  $\Phi(\vec{r})$  can be described by the following equation:

$$\nabla\Phi(\vec{r}) = \vec{K}_k(\vec{r}) \quad (13)$$

Then, the WPF  $\Gamma(\vec{r})$  can be reformulated as:

$$\Gamma(\vec{r}) = \frac{1}{2} + \frac{1}{2} \cos(P\nabla\Phi(\vec{r}) \cdot \vec{r}) \quad (14)$$

To solve Eq. (13), there are many different numerical approaches. In this paper, the finite-difference method is introduced to approximate the gradient of a phase field [49]. During solving Eq. (13), a least-square approach is applied here. The formulation of the least square approach can be expressed as:

$$\min_{\Phi(\vec{r})} : L(\Phi(\vec{r})) = \int_{\Omega} \left\| \nabla\Phi(\vec{r}) - \vec{K}_k(\vec{r}) \right\|_2^2 d\Omega \quad (15)$$

By solving the problem defined from Eq. (15), the mapping phase function  $\Phi(\vec{r})$  can be established. However, the least square solution of Eq. (15) will lead to the non-negligible angle discrepancy between  $\nabla\Phi(\vec{r})$  and  $\vec{K}_k(\vec{r})$  in the high-stress region (shown in Fig. 6(a)), which may significantly weaken the mechanical performance of fabricated

structures. To ameliorate this issue, a constrained least-squares formula is added to Eq. (15) which can force the infill path to strictly follow the principal stress on high-stress regions. Then the Eq. (15) can be reformulated as the following:

$$\begin{aligned} \min_{\Phi(x,y)} : L(\Phi(\vec{r})) &= \int_{\Omega} \left\| \nabla\Phi(\vec{r}) - \vec{K}_k(\vec{r}) \right\|^2 d\Omega \\ \text{s.t.} : \quad \nabla\Phi(\vec{r}) \cdot \vec{f}_k(\vec{r}) &= 0 \end{aligned} \quad (16)$$

Let  $d = 8$ , the result of Eqs. (16) and (14) shows local frequency incoordination (Fig. 6(b)), so it is necessary to construct penalty terms to relax constraints in low-stress regions. Since the value of stress varies by several orders of magnitude at different positions in finite element analysis, the sort transformation is utilized to process the stress field. To construct this penalty term, the design space has been divided into two sub-regions based on the sorted principle stress field  $S(\vec{r})$ .  $S(\vec{r})$  and sub-regions  $\Omega_u, \Omega_r$  are defined as:

$$S(\vec{r}) = \begin{cases} 0 & \sigma(\vec{r}_1) = \min\{\sigma(\vec{r})\}, i = 1 \\ \frac{i-1}{N-1} & \sigma(\vec{r}_{i-1}) \leq \sigma(\vec{r}_i) \leq \sigma(\vec{r}_{i+1}), 1 < i < N-1 \\ 1 & \sigma(\vec{r}_N) = \max\{\sigma(\vec{r})\}, i = N \end{cases} \quad (17)$$

$$\begin{aligned} \Omega_u &= \{\vec{r} \in \Omega | S(\vec{r}) \geq 0.5\} \\ \Omega_r &= \{\vec{r} \in \Omega | S(\vec{r}) < 0.5\} \end{aligned} \quad (18)$$

where  $N$  is the number of gross elements. Based on this division, a new least square formulation with penalty term can be formulated as:

$$\begin{aligned} \min_{\Phi(x,y)} : L(\Phi(\vec{r})) &= \int_{\Omega} \left\| \nabla\Phi(\vec{r}) - \vec{K}(\vec{r}) \right\|^2 d\Omega \\ \text{s.t.} : \quad \int_{\Omega_u} \left\| \nabla\Phi(\vec{r}) \cdot \vec{f}(\vec{r}) \right\|^2 d\Omega &= 0 \end{aligned} \quad (19)$$

The result of Eqs. (19) and (14) can both decrease the discrepancy between  $\Phi(\vec{r})$  and  $\vec{K}_k(\vec{r})$  while avoiding high-frequency turbulence (shown in Fig. 6(c)). However, it may also lead to undesirable distortion or fluctuation in low-stress regions.

#### 2.5. Infill trajectory extraction

This section aims to convert projection from the wave projection function  $\Gamma(\vec{r})$  to a 0–1 dual-phase projection function  $\Gamma_r(\vec{r})$  and extract streamlines to generate printing paths (shown in Fig. 7(a)). The dual-phase projection function  $\Gamma_r(\vec{r})$  is defined as follows:

$$\Gamma_r(\vec{r}) = \begin{cases} 1 & \text{if } \Gamma(\vec{r}) \geq T_r \\ 0 & \text{if } \Gamma(\vec{r}) < T_r \end{cases} \quad (20)$$

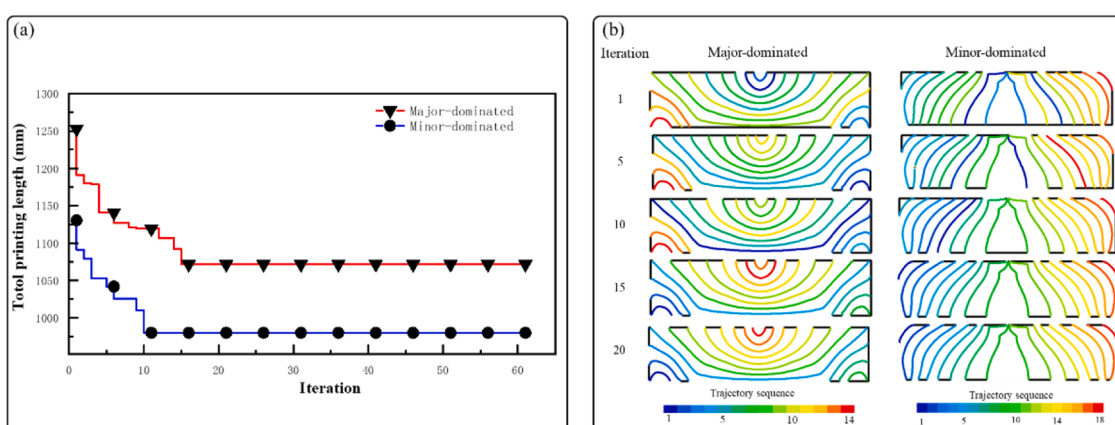
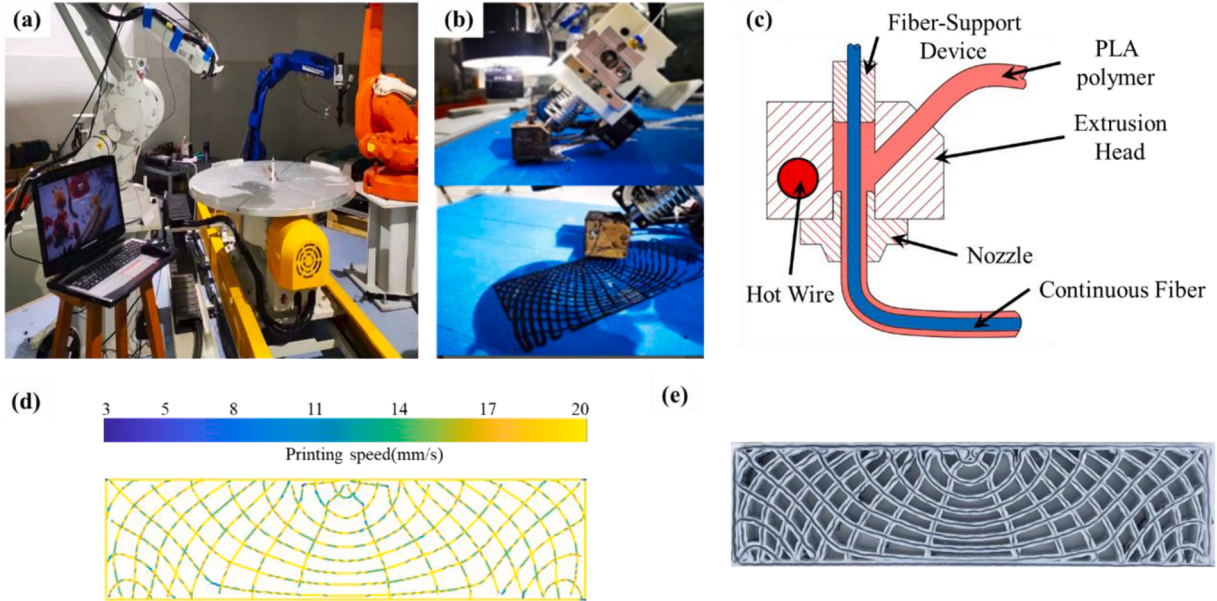


Fig. 8. (a) Convergence curve utilizing SA for total printing length; (b) Convergence state for specific iteration steps about two toolpath segments.



**Fig. 9.** (a) ABB robot-based system for 3D-printed CFRP; (b) Extrusion system for 3D-printed CFRP; (c) The schematic of the extrusion system for 3D-printed CFRP; (d) The printing speed of connected trajectory; (e) The Stress-driven infill composites structure.

**Table 1**  
Moving speed mapping with respect to toolpath tuning angle.

Local tuning angle (°)	0–10	10–20	20–30	30–40	40–50	50–60	> 60
Moving speed (mm/s)	20	17	14	11	8	5	3

In this work, the threshold value  $T_r$  is 0.85 (usually 0.8–0.9). The results are shown in Fig. 7(c). A streamline approach is utilized to extract the streamline from the binary image to generate the infill path for the printing process. Streamlines are tangent to the vector field; The streamline function  $\psi(\vec{r})$  is obtained by the following minimization scheme:

$$\min : I(\psi) = \frac{1}{2} \int_{\Omega} \Gamma_r(\vec{r}) |\nabla \times \psi - \vec{K}(\vec{r})| d\Omega \quad (21)$$

As shown in Fig. 7(d), streamlines extracted from the dual-phase projection are feasible for manufacturing and will be utilized to generate infill printing paths.

## 2.6. Toolpath connection

In this work, cutting points of fibers due to discontinuation of the infill path are avoided by connecting the two endpoints of two different infill printing paths along the boundary of the design space. The connected toolpath on the boundary can be considered as the outer contour of the design space. It should be noticed that a certain segment on the

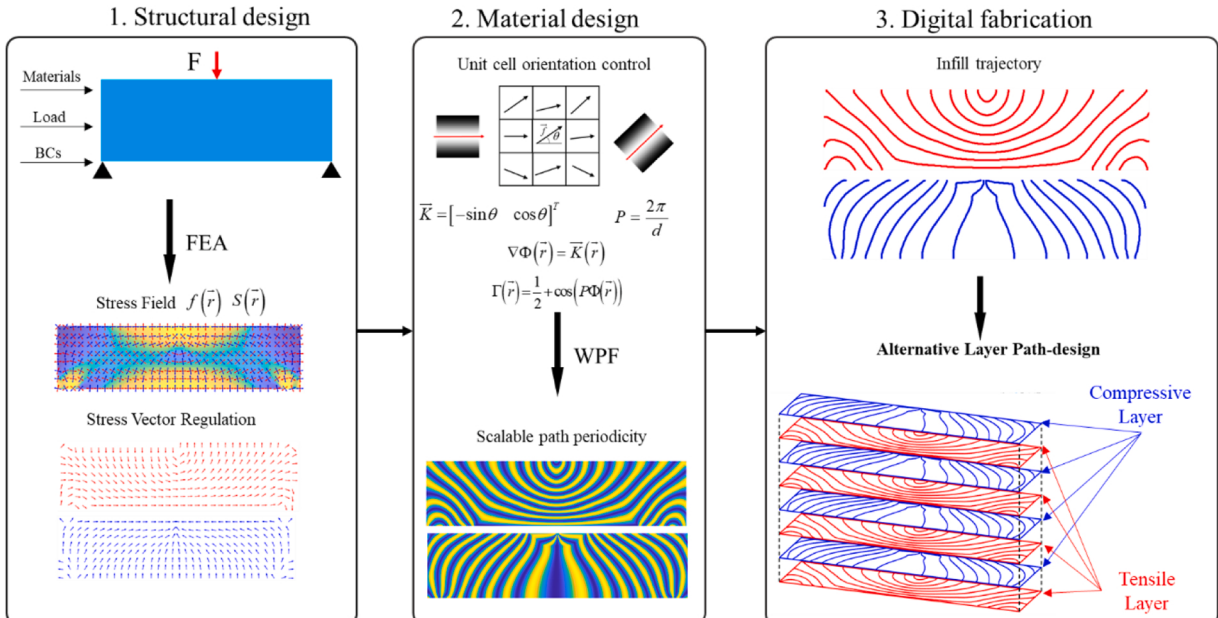


**Fig. 10.** Infill pattern and path generation of continuous fiber AM in MBB.

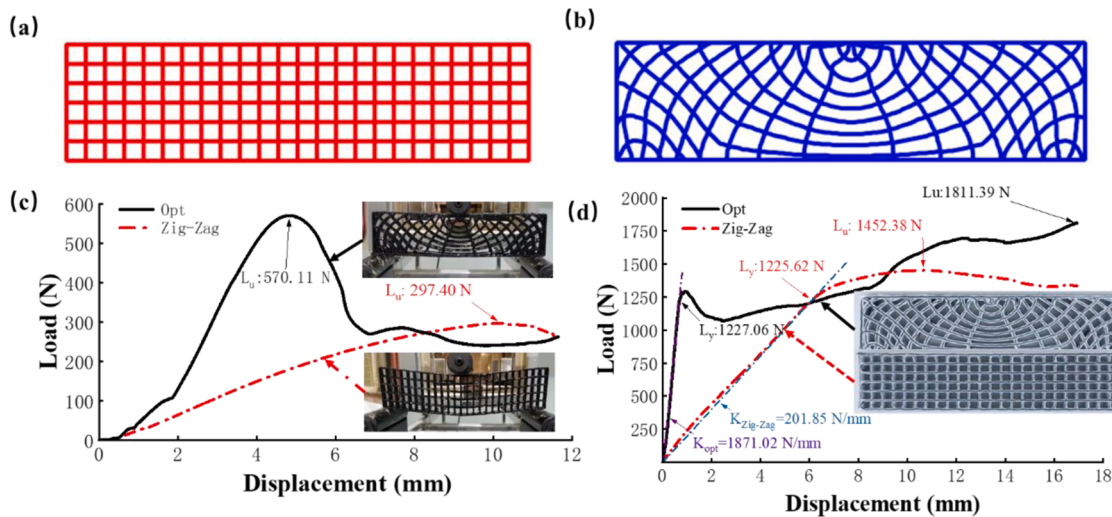


**Fig. 11.** (a) Zig-Zag infill trajectory; (b) Stress-driven projection trajectory; (c) Stress-driven projection vs Zig-Zag (Polymer structure via FDM); (d) Stress-driven projection and Zig-Zag infill for CFRP structure.

boundary might be printed more than one time. In this case, an offset of the path is set to avoid the intersection. Here, although the elimination of cutting points can be realized by the printing method mentioned above, different printing sequences of toolpath will produce different total printing lengths and the optimal or shortest total printing length is expected.

Let  $\mathbf{G} = (\mathbf{V}, \mathbf{E})$  be an undirected graph with the set of vertices  $\mathbf{V}$  and set of edges  $\mathbf{E} = \{(x, y) | (x, y) \in \mathbf{V}\}$ . In this paper, the vertices set  $\mathbf{V}$  includes all the start or end vertices on the toolpath segments generated from the previous steps. Let the set of vertices be  $\mathbf{V} = \{v_1, v_2, \dots, v_n\}$ . We define the cost matrix  $\mathbf{C}$  by

$$\mathbf{C} = (c_{ij})_{n \times n} \quad (22)$$

$$c_{ij} = \begin{cases} l_{ij}, e_{ij} \in T_s \\ p_{ij}, e_{ij} \notin T_s \end{cases} \quad (23)$$

where  $e_{ij}$  is the edge in set  $\mathbf{E}$  which connects vertex  $v_i$  and  $v_j$ .  $T_s$  is the set of edges that are generated in the previous steps for infill.  $l_{ij}$  is the length of the infill segment while  $p_{ij}$  is the shortest length that can connect  $v_i$  and  $v_j$  along the boundary of infill space. To describe the infill sequence, decision variables  $y_{ij}$  for each edge  $e_{ij}$  such that

$$y_{ij} = \begin{cases} 1 & \text{path is linked from } i \text{ to } j \\ 0 & \text{otherwise} \end{cases} \quad (24)$$

The toolpath connection problem can be formulated as an optimization problem stated below:

$$\begin{aligned} \text{Min : } & \sum_i \sum_j c_{ij} y_{ij} \\ \text{s.t. : } & \{ \quad \sum_i y_{ij} = 1 \quad \sum_j y_{ij} = 1 \quad \sum_{(i,j) \in T_s} y_{ij} + \sum_{(i,j) \in T_s} y_{ji} = n(T_{ij}) \end{aligned} \quad (25)$$

where  $n(T_{ij})$  is the number of edges in the set  $T_{ij}$ . This is a classical optimization problem named Travelling Salesman Problems (TSP). TSP is a Non-Deterministic Polynomial-time hard (NP-hard) problem, there are many studies focused on solving it [50–52]. Proposed by Kirkpatrick et al. [53], SA is an effective optimization method to solve a combinatorial optimization problem and easily be implemented and extended to new problems. In this work, the classical SA method is used to solve the defined optimization problem. The order of the printing paths can be determined by the order of the points. The optimization of the iteration process for total printing distance and the continuous tool path is shown

in Fig. 8. Ultimately, the sequence of printing paths maintaining minimal total print length tool path is generated.

## 2.7. Experimental fabrication

A 6-DOF robot-based system is designed for continuous fiber composite fabrication in a layer-by-layer manner (shown in Fig. 9(a)). The extrusion system is to drive thermoplastic filament into the nozzle and achieve in-situ impregnation of fiber bundles (Fig. 9(b) and (c)). The nozzle diameter is 1.2 mm and polylactic acid (PLA) polymer filament is selected as the feeding material. The fiber bundle (T300, 1 K, Toray Industries, Inc. from Japan) is used for the printing process.

The toolpath with sequential lines is fitting into the program of robot motion control. The software for ABB robot and printer head control was developed using Python App Designer and it provides users with two main functionalities: (i) robot code generation; (ii) process monitoring. The points of  $[x, y, z]$  coordinate value can be converted to robot code and fit into a linear Move command in ABB's RAPID language corresponding to identical coordinates. It is important to have the same reference frame via Tool Center Point (usually bed origin) defined in the robot program. The parameters used to define the linear motion in the RAPID command as *MoveTo Point, Speed, Zone, Tool[\Wobj]*, where “ToPoint” is the target point defined with the reference coordinate system; “Speed” indicates the velocity of the linear movements of the printer head.

To ensure the accurate fiber trajectory, the process parameters are dynamically changed concerning the toolpath turning angle between two adjacent directional vectors, among three printing points, in the trace. When the nozzle goes through the large curvature line or typical tuning point, its moving speed needs to be slowed down. The moving speed is set to fit with the local tuning angle of the toolpath as follows in Table 1. The feeding speed is adjusted to ensure a constant extrusion speed.

As shown in Fig. 9(b), the printing speed of the fiber trajectory is distributed according to its turning angle. The speed is higher at the place where the track is flat, and lower at the place where the turning angle is large and the speed transition follows the law of simple harmonic motion to avoid significant vibration. As shown in Fig. 9(c), the Stress-driven infill composite structure is manufactured based on the printing robot system and variable printing speed.

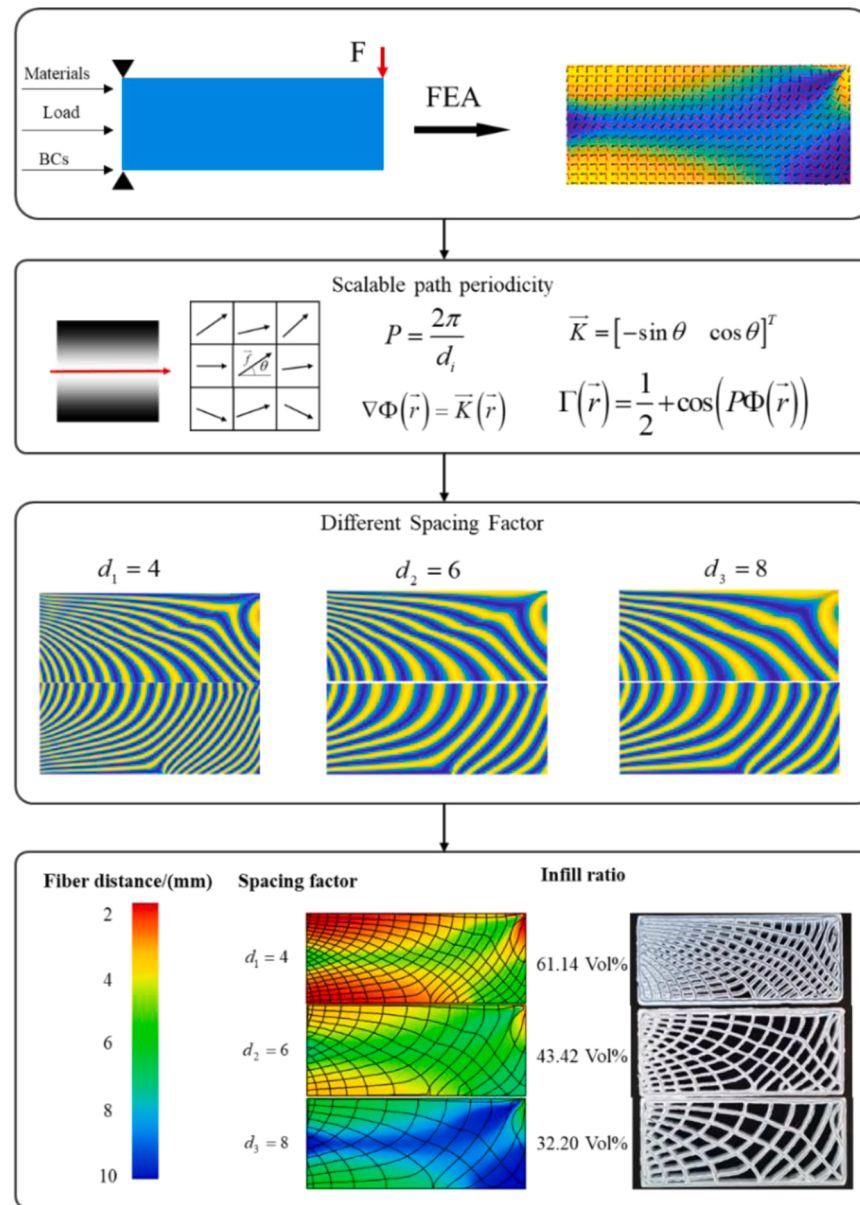


Fig. 12. Infill pattern and path generation of CFRP via AM in a cantilever plate by monitoring the infill space factor.

### 3. Results and discussion

#### 3.1. Infill path

The proposed to design stress-driven infill path is to improve structural load-bearing and achieve quantitative control of the infill ratio. At first, a three-points-bending bridge loading analysis is conducted and then the continuous fiber path can be generated by the proposed approach to infill the confined rectangle design area following the field function  $\Gamma(\vec{r})$ . The projection algorithm is employed to align the fiber path with tensile or compressive stress vectors in each element of MBB. An alternate compressive-tensile infill strategy is implemented for toolpath generation as illustrated in Fig. 10. For comparison, the zigzag infill pattern is designed with an identical infill ratio to the stress-driven projection toolpath (shown in Fig. 11 (a) and (b)). The infill ratio  $Ir$  is defined as follows:

$$Ir = \frac{w \times \sum_{i=1}^N L_i}{A} \times 100\% \quad (26)$$

where  $w$  is the width of the path,  $N$  is the number of trajectories,  $L_i$  is the length of the individual path, and  $A$  is the total area of design space. In general, the interspace between two fiber trajectories should be larger than the width of the path, then the adjacent distance of fibers should be set greater than  $w$ .

In order to evaluate the mechanical enhancement of continuous carbon fiber, the 3D-printed specimens with and without reinforcements are fabricated and measured by three-bending-point testing. The resultant force-displacement curves show that stress-driven projection design exhibits a significant improvement in mechanical stiffness and strength (Fig. 11 (c)). The ultimate load stress-driven projection achieves 570.11 N, which is nearly double as compared with 297.40 N of the zigzag infill design. Brittle fractures at the local infill path are observed in the plastic specimen especially in the zigzag pattern. Moreover, with the enhancement of carbon fiber, the composite specimens of stress-driven projection and zigzag infill pattern show the maximum ultimate load of 1811.39 N and 1452.38 N respectively (Fig. 11 (d)).

The slope of force-displacement curves obtained from stress-driven infill (1871.02 N/mm) is much steeper than that of load-independent

zigzag infill (201.85 N/mm). The yield loads are 1227.06 N and 1225.62 N with respect to the stress-driven infill pattern and zig-zag infill pattern which reveals that the stress-driven infill specimen reaches its yielding load later than its counterpart. However, the structure still maintains relatively high load resistance, and its stress gradually raises to ultimate strength value until its material is densified. Whereas, the zig-zag specimen shows different deformation behavior where stress slowly reaches the yield stress, and then dramatically drops due to local fractures or collapse of fiber patterns. As the loading process continued, the bearing capacity of the material gradually increased and eventually exceeded the Zig-Zag infill pattern specimen. Thus, the stress-driven infill pattern exhibits excellent stiffness and strong loading resistance, and it indicated that the proposed infill strategy is much effective to improve the elastic mechanical performance rather than the compliance and plastic strength. Once the composite structures experience large local deformation, large compliance and plastic strength are observed in both types of design patterns.

### 3.2. Infill ratio

Apart from infill path, infill ratio is also a significant factor for monitor the infill pattern design, which influences the mechanical performance of composite structures. The field function  $\Gamma(\vec{r})$  is associated with the scalar variable of periodicity  $P$  and spatially variant direction vector field  $\vec{K}$ . The infill strategy of stress-driven projection is able to monitor the infill density based on the spacing factor  $d$ , which is reversely proportional to the periodicity  $P$ . Thus, with the spacing factor  $d$  increasing, the entire infill density, as well as the length of the infill line, also reduces correspondingly (Fig. 12).

The contour and infill patterns are created by streamline extraction to map with the stress-intensive region (Fig. 12). For a cantilever plate, the spacing factor  $d$  is the design variable to be tuned by users. The minimum line spacing is set as 1.2 mm and  $d$  is set as 4, 6 and 8 to monitor the infill density in the fixed region of the cantilever plate. Three designs with different infill densities (Fig. 12) are fabricated by continuous carbon fiber 3D printing, and the printing speed mapping is properly introduced to ensure the accurate location of carbon fibers. The force-displacement curves of this batch specimen illustrate that the load-bearing capability improved from 192.05 N to 723.35 N as the infill spacing factor reduces from 8 to 4, correspondingly (Fig. 13). Whereas, the slopes of force-displacement curves of three specimens show a slight variance in the small displacement region, and it indicates that the stress dissipation is addressed on the fixed node of the cantilever plate at starting region. As the vertical displacement increases, the entire structure goes to sustain the external loading and the load-bearing capability of the three specimens gradually varies. The maximum load of the composite structure is strongly associated with the spacing factor

structure is illustrated in this section. Topology optimization (TO) is a well-known design method to obtain material distribution. Proposed by Bendsøe et al., the density method is formulated for TO [54], and SIMP (Solid Isotropic Material with Penalization) proves to be an efficient method to solve TO problems and maintain clear optimal topologies structures for isotropic materials [55]. Similarly, SOMP (Solid Orthotropic Material with penalization) is utilized for optimizing the orthotropic material distribution and direction in this case. The process of optimization is based on FEM and iterative design variables (Fig. 14).

Design variables were defined as follows:

$$\mathbf{X} = \{\rho_1, \dots, \rho_N; \theta_1, \dots, \theta_N\} \quad (27)$$

where  $\rho_i$  is the pseudo-density value of the  $i$ -th element and  $\theta_i$  is the orientation of the  $i$ -th element.  $N$  is the total number of elements. The global stiffness matrix  $\mathbf{K}$  is assembled by the element stiffness matrix  $\mathbf{k}_i(\rho_i, \theta_i)$ :

$$\mathbf{K} = \sum_{i=1}^N \mathbf{k}_i(\rho_i, \theta_i) \quad (28)$$

The  $i$ -th element stiffness matrix  $\mathbf{k}_i(\rho_i, \theta_i)$  is formulated as

$$\mathbf{k}_i(\rho_i, \theta_i) = \int_{\Omega_i} \mathbf{B}^T \mathbf{D}(\rho_i, \theta_i) \mathbf{B} d\Omega_i \quad (29)$$

where  $\mathbf{B}$  is the strain-displacement matrix,  $\Omega_i$  is the design domain contained in  $i$ -th element;  $\mathbf{D}(\rho_i, \theta_i)$  is the elastic matrix with orientation and pseudo-density; the SOMP is used as the material interpolation model. The rotation relationship is conducted by the transformation matrix  $\mathbf{R}(\theta)$ . The elastic matrix  $\mathbf{D}(\rho_i, \theta_i)$  is defined as

$$\mathbf{D}(\rho_i, \theta_i) = \rho_i^p \mathbf{R}(\theta_i)^T \mathbf{D} \mathbf{R}(\theta_i) \quad (30)$$

where  $p$  is the penalty factor and compliance matrix  $[\mathbf{D}]^{-1}$  is:

$$[\mathbf{D}]^{-1} = \begin{bmatrix} \frac{1}{E_1} & \frac{-v_{12}}{E_1} & 0 \\ \frac{-v_{21}}{E_2} & \frac{1}{E_2} & 0 \\ 0 & 0 & \frac{1}{G_{12}} \end{bmatrix} \quad (31)$$

and the transformation matrix  $\mathbf{R}(\theta)$  is:

$$\mathbf{R}(\theta) = \begin{bmatrix} \cos^2 \theta & \sin^2 \theta & \cos \theta \sin \theta \\ \sin^2 \theta & \cos^2 \theta & -\cos \theta \sin \theta \\ -2 \cos \theta \sin \theta & 2 \cos \theta \sin \theta & \cos^2 \theta - \sin^2 \theta \end{bmatrix} \quad (32)$$

The optimization formulation coupled with density and material direction can be mathematically formulated as follows:

$$\text{Find : } \mathbf{X} = \{\rho_1, \dots, \rho_N; \theta_1, \dots, \theta_N\}$$

$$\min_{\rho, \theta} : c(\rho, \theta) = \mathbf{U}^T \mathbf{K} \mathbf{U} = \sum_{i=1}^N \mathbf{u}_i^T \mathbf{k}_i(\rho_i, \theta_i) \mathbf{u}_i \quad \text{Subjected to : } \left\{ \mathbf{K} \mathbf{U} = \mathbf{F} \frac{V(\rho, \theta)}{V_D} \leq V_f \right. \quad (33)$$

of infill density. This implies that stress-driven projection is an effective approach to modifying the infill density and the infill path for composite structure development.

### 3.3. Adaptive infill mapping for topology optimized structure

For the capability of stress-driven projection for structures with complex configurations, the infill design coupled with topology

where  $c$  represents the compliance of the structure;  $\mathbf{K}$  and  $\mathbf{U}$  are global stiffness matrix and displacement vector, respectively;  $\mathbf{u}_i$  is the element displacement vector with respect to  $i$ -th element;  $\rho_{\min}$  (usually set as 0.001) is a small positive number as the lower bound to avoid the singularity.  $V_D$  is the volume of the design domain,  $V(\rho, \theta)$  is the material volume, and  $V_f$  is the volume fraction.

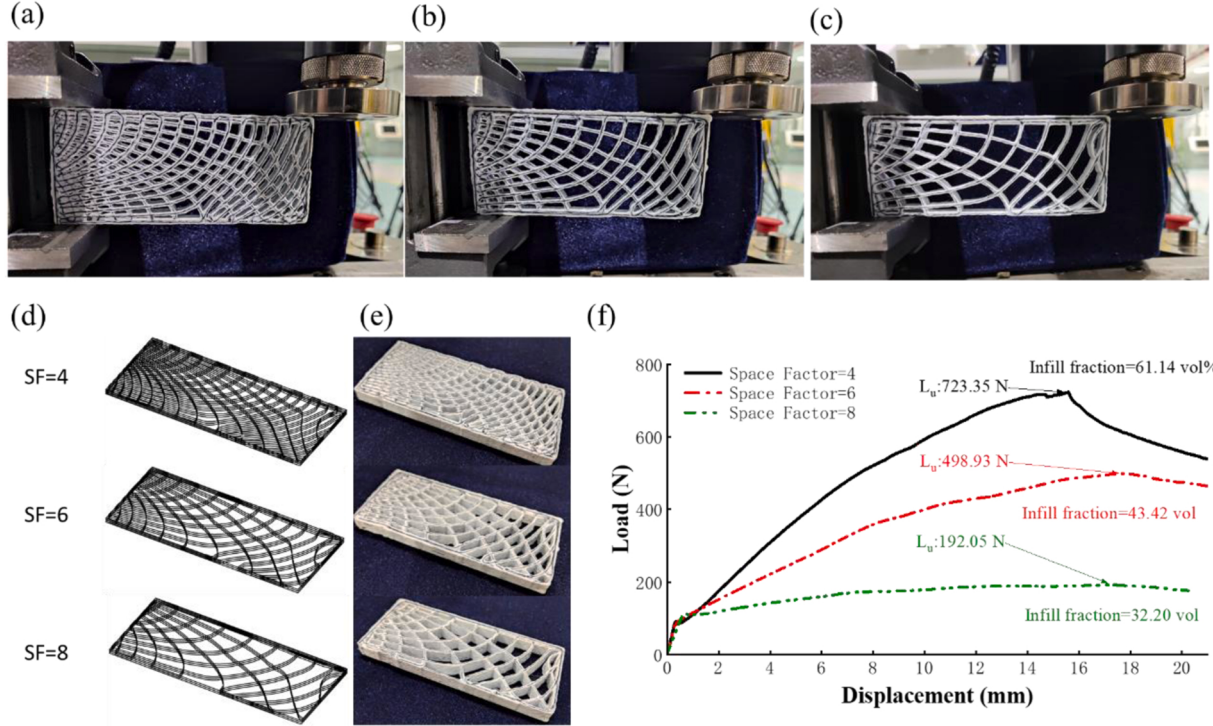


**Fig. 13.** Experimental investigation of designed specimens: (a) cantilever testing for SF = 4; (b) cantilever testing for SF = 6; (c) cantilever testing for SF = 8; (d) and (e) Design and printed cantilever specimens with respect to varied space factors; (f) Force-displacement curves of cantilever specimens with different infill ratio.

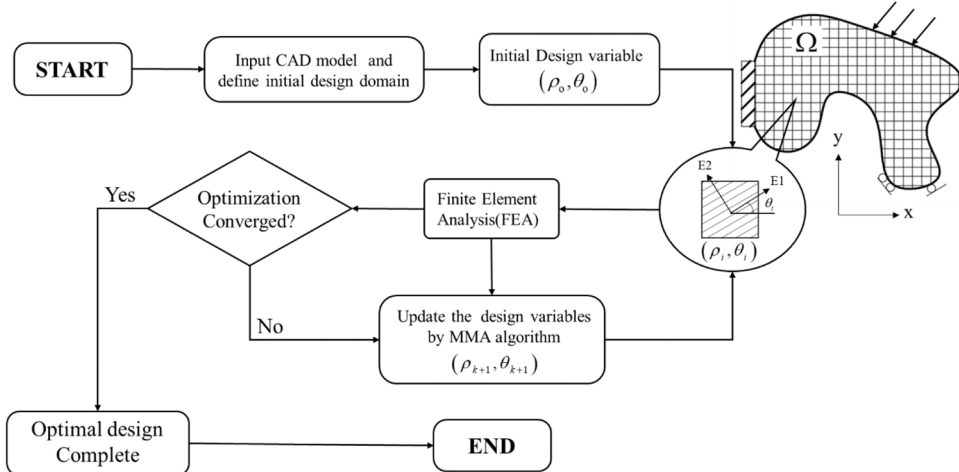


**Fig. 14.** Flowchart of solving the optimization method.

The optimization problem is solved iteratively by the gradient-based optimization algorithms named Method of Moving Asymptotes (MMA) which is used to update the design variable [56,57]. For the sensitivity analysis of the objective and constraint function with respect to design variables  $\rho_i$  and  $\theta_i$ , the details are shown in Appendix. The process of the optimization method for structures of orthotropic materials is integrated into a flowchart shown in Fig. 14.

Fig. 15 (a) shows the geometric dimension, load, boundary conditions, and material orientation schematic of the MBB beam. The polymer-capsulated fiber bundle possesses orthotropic properties. Its material properties,  $E_1$ ,  $E_2$ ,  $v_{12}$  and  $G_{12}$  are 80.0 GPa, 30.5 GPa, 0.33, and 30.1 GPa respectively. As for the loading condition, it is loaded with  $F = 30\text{N}$ . The volume fraction  $V_f$  is set as 50 %. Fig. 15 (b) shows the structure compliance curve of iterative optimization and the volume fraction. Fig. 15 (c) shows the final topologized structure with

compliance value of 81.17 mJ. The local density and stress orientation are obtained and used for infill mapping by the wave projection approach. The stress intensity and vector fields are used to guide the local infill density and fiber orientation simultaneously. The infill toolpath and speed mapping trajectory are generated by coupling the tensile-compressive stresses dominated field and corresponding to the moving speed mapping (Fig. 15 (d)-(f)).

Differing from the regular infill areas, it is hard to generate a continuous toolpath infilling the whole topology area without cutting. In this work, a multi-group printing method is proposed to carry out the printing process. For trajectories in each group, the toolpath connection discussed in Section 2.6 is carried out to combine multiple trajectories into one continuous toolpath. In this case, all trajectories are divided into 10 groups (shown in Fig. 16 (a)). The details of the groups' situation are shown in Fig. 16 (b). Based on the equipment illustrated in Section

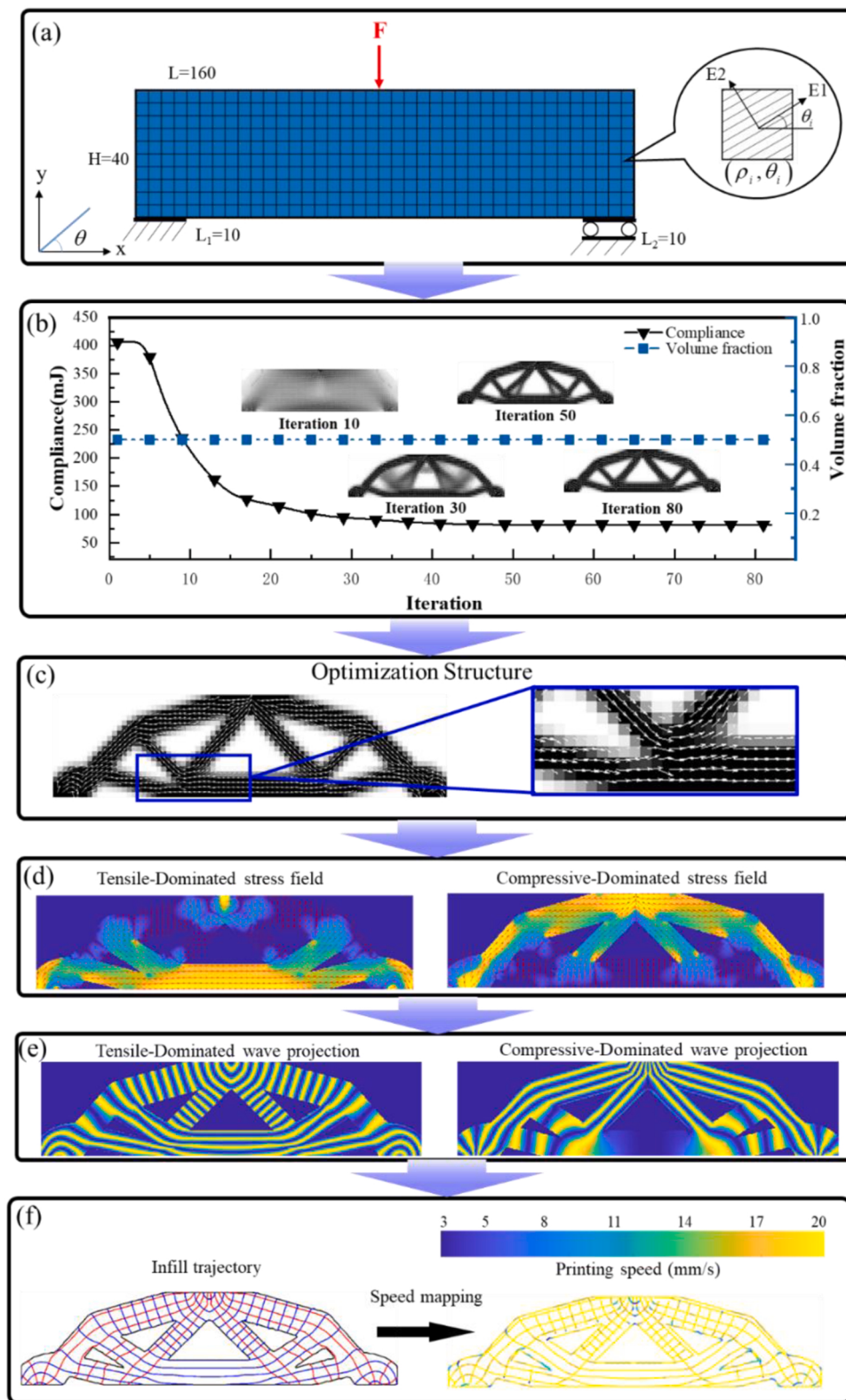


**Fig. 15.** Topology infill path and path generation of continuous fiber AM for MMB.

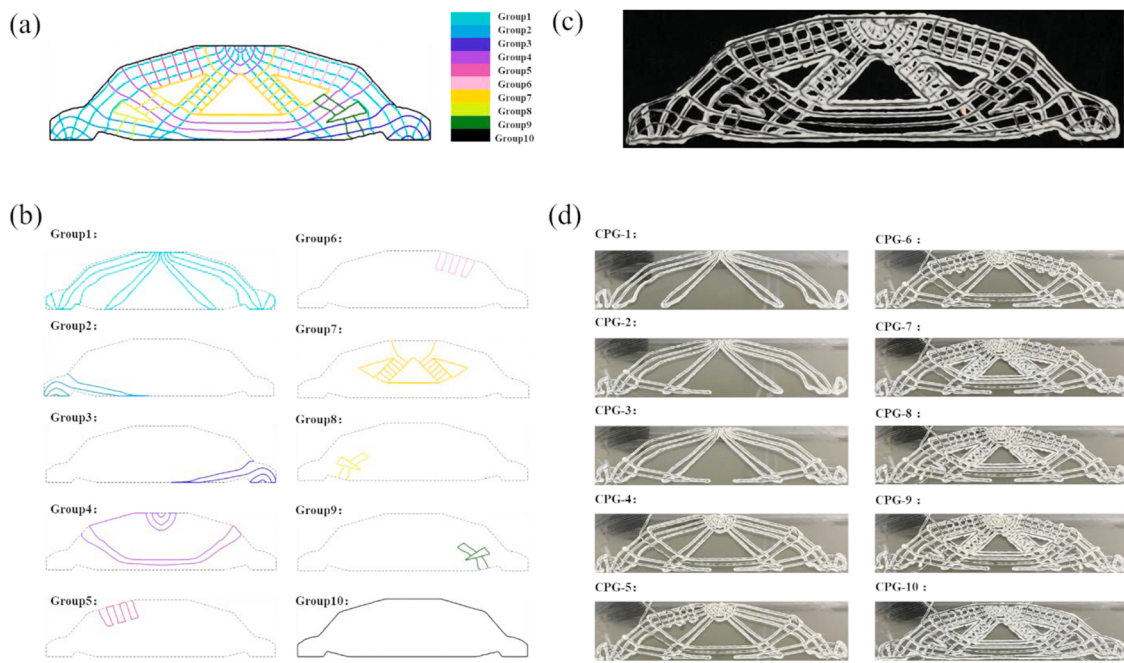


**Fig. 16.** (a) Overall grouping diagram; (b) Diagram of each group; (c) Printed topology optimized MBB beam with CFRP; (d) The picture after each group toolpath was completed about the topology-optimized MBB beam.

2.7, the topology structure is printed according to the trajectory designed by the multi-group printing method (shown in Fig. 16 (c)). Pictures of each completed printing group (CPG) are listed in Fig. 16 (d).

#### 4. Conclusion

A stress-driven infill mapping approach for 3D-printed continuous fiber composite is developed to form conformable infill pattern with stress-driven infill path and tunable intensity. The infill density corresponding to different loads can be generated by controlling the design parameter (i.e. the spacing factor). The wave projection method is helpful to align the fiber with the local stress vector and map the infill spacing with local stress intensity, so as to achieve adaptive infill patterns. Topology optimization via SOMP is introduced to describe the anisotropic fiber elemental behavior and MMA is applied to concurrently optimize the entire structure of MMB and generate the infill pattern coupled with the stress-driven approach. The fiber path induced by wave projection behaves as a skeleton to enhance the structural mechanical performance. TSP-based path planning algorithm is employed to complete the toolpath connection and minimize cutting points and traveling distance. This generalized periodic design of infill mapping can fully exploit the anisotropic properties of fiber bundles as well as improve the lightweight performance of composite structures via AM.

#### Appendix

For the gradient-based optimization algorithms, the derivatives of the objective function and constraint function must be needed to be provided with respect to design variables through sensitivity analysis. The sensitivity analysis is conducted as

$$\left\{ \begin{array}{l} \frac{\partial c}{\partial \rho_i} = \frac{\partial (\mathbf{U}^T \mathbf{K} \mathbf{U})}{\partial \rho_i} \\ \frac{\partial c}{\partial \theta_i} = \frac{\partial (\mathbf{U}^T \mathbf{K} \mathbf{U})}{\partial \theta_i} \end{array} \right. \quad (34)$$

For the objective function  $c$ , the first-order derivative with respect to  $\rho_i$  can be written as:

$$\frac{\partial(\mathbf{U}^T \mathbf{K} \mathbf{U})}{\partial \rho_i} = 2 \mathbf{U}^T \mathbf{K} \frac{\partial \mathbf{U}}{\partial \rho_i} + \mathbf{U}^T \frac{\partial \mathbf{K}}{\partial \rho_i} \mathbf{U} \quad (35)$$

For  $\frac{\partial \mathbf{U}}{\partial \rho_i}$ , considering the finite element equation

$$\mathbf{K} \mathbf{U} = \mathbf{F} \quad (36)$$

The differential of Eq. (36) with respect to  $\rho_i$  can be written as

$$\frac{\partial \mathbf{K}}{\partial \rho_i} \mathbf{U} + \mathbf{K} \frac{\partial \mathbf{U}}{\partial \rho_i} = \frac{\partial \mathbf{F}}{\partial \rho_i} \quad (37)$$

For the load-independent problem,  $\mathbf{F}$  is a constant value, it satisfies  $\frac{\partial \mathbf{F}}{\partial \rho_i} = 0$ . Therefore

$$\frac{\partial \mathbf{U}}{\partial \rho_i} = - \mathbf{K}^{-1} \frac{\partial \mathbf{K}}{\partial \rho_i} \mathbf{U} \quad (38)$$

Combining Eq. (35) and Eq. (38), the first-order derivative of the objective function  $c$  with respect to  $\rho_i$  can be expressed as

$$\frac{\partial c}{\partial \rho_i} = - \mathbf{U}^T \frac{\partial \mathbf{K}}{\partial \rho_i} \mathbf{U} = - \mathbf{u}^T \frac{\partial \mathbf{k}_i(\rho_i, \theta_i)}{\partial \rho_i} \mathbf{u} \quad (39)$$

Combining Eq. (29),

$$\frac{\partial c}{\partial \rho_i} = - \mathbf{u}_i^T \frac{\partial \int_{\Omega_i} \mathbf{B}^T \mathbf{D}(\rho_i, \theta_i) \mathbf{B} d\Omega_i}{\partial \rho_i} \mathbf{u}_i = - \mathbf{u}_i^T \int_{\Omega_i} \mathbf{B}^T \frac{\partial \mathbf{D}(\rho_i, \theta_i)}{\partial \rho_i} \mathbf{B} d\Omega_i \mathbf{u}_i \quad (40)$$

repeat the steps from (35)–(40), the derivative of the objective function  $c$  with respect to  $\theta_i$  is:

$$\frac{\partial c}{\partial \theta_i} = - \mathbf{u}_i^T \int_{\Omega_i} \mathbf{B}^T \frac{\partial \mathbf{D}(\rho_i, \theta_i)}{\partial \theta_i} \mathbf{B} d\Omega_i \mathbf{u}_i \quad (41)$$

according to Eq. (30) and Eq. (32), the derivative of the elastic matrix  $\mathbf{D}(\rho_i, \theta_i)$  with respect to  $\rho_i$  and  $\theta_i$  are as follows:

$$\begin{cases} \frac{\partial \mathbf{D}(\rho_i, \theta_i)}{\partial \rho_i} = p \rho_i^{p-1} \mathbf{R}(\theta_i)^T \mathbf{D} \mathbf{R}(\theta_i) \\ \frac{\partial \mathbf{D}(\rho_i, \theta_i)}{\partial \theta_i} = \rho_i^p \left[ \frac{\partial \mathbf{R}(\theta_i)^T}{\partial \theta_i} \mathbf{D} \mathbf{R}(\theta_i) + \mathbf{R}(\theta_i)^T \mathbf{D} \frac{\partial \mathbf{R}(\theta_i)}{\partial \theta_i} \right] \end{cases} \quad (42)$$

The derivative of material volume  $V(\rho, \theta)$  with respect to  $\rho_i$  and  $\theta_i$  is as follows:

$$\begin{cases} \frac{\partial V(\mathbf{X})}{\partial \rho_i} = \frac{\rho_i}{V_D} \\ \frac{\partial V(\mathbf{X})}{\partial \theta_i} = 0 \end{cases} \quad (43)$$

## References

- [1] S. Yuan, S. Li, J. Zhu, Y. Tang, Additive manufacturing of polymeric composites from material processing to structural design, Composites Part B: Engineering 219 (2021) 108903.
- [2] D.P. Cole, T.C. Henry, F. Gardea, R.A. Haynes, Interphase mechanical behavior of carbon fiber reinforced polymer exposed to cyclic loading, Composites Science and Technology 151 (2017) 202–210.
- [3] Z. Xu, C.S. Ha, R. Kadam, J. Lindahl, S. Kim, H.F. Wu, V. Kunc, X. Zheng, Additive manufacturing of two-phase lightweight, stiff and high damping carbon fiber reinforced polymer microlattices, Additive Manufacturing 32 (2020) 101106.
- [4] Y. Zhang, W. Tao, Y. Zhang, L. Tang, J. Gu, Z. Jiang, Continuous carbon fiber/crosslinkable poly (ether ether ketone) laminated composites with outstanding mechanical properties, robust solvent resistance and excellent thermal stability, Composites Science and Technology 165 (2018) 148–153.
- [5] W. De Backer, A.P. Bergs, M.J. Van Tooren, Multi-axis multi-material fused filament fabrication with continuous fiber reinforcement, 2018 AIAA/ASCE/AHS/ASC Structures, Structural Dynamics, and Materials Conference, 2018, p. 0091.
- [6] C. Quan, B. Han, Z. Hou, Q. Zhang, X. Tian, T.J. Lu, 3d printed continuous fiber reinforced composite auxetic honeycomb structures, Composites Part B: Engineering 187 (2020) 107858.
- [7] H. Awais, Y. Nawab, A. Amjad, A. Anjum, H.M. Akil, M.S.Z. Abidin, Environmental benign natural fibre reinforced thermoplastic composites: A review, Composites Part C: Open Access 4 (2021) 100082.
- [8] M. Hassan, A. Othman, S. Kamaruddin, A review on the manufacturing defects of complex-shaped laminate in aircraft composite structures, The International Journal of Advanced Manufacturing Technology 91 (9) (2017) 4081–4094.
- [9] F. Raspall, R. Velu, N.M. Vaheed, Fabrication of complex 3D composites by fusing automated fiber placement (AFP) and additive manufacturing (AM) technologies, Advanced Manufacturing: Polymer & Composites Science 5 (1) (2019) 6–16.
- [10] M. Torres, Parameters' monitoring and in-situ instrumentation for resin transfer moulding: A review, Composites Part A, Applied Science and Manufacturing 124 (2019) 105500.
- [11] X. Wang, M. Jiang, Z. Zhou, J. Gou, D. Hui, 3D printing of polymer matrix composites: A review and prospective, Composites Part B: Engineering 110 (2017) 442–458.
- [12] S.D. Nath, S. Nilufar, An overview of additive manufacturing of polymers and associated composites, Polymers 12 (11) (2020) 2719.
- [13] M.-P. Schmidt, L. Couret, C. Gout, C.B. Pedersen, Structural topology optimization with smoothly varying fiber orientations, Structural and Multidisciplinary Optimization 62 (6) (2020) 3105–3126.
- [14] V.S. Papapetrou, C. Patel, A.Y. Tamjani, Stiffness-based optimization framework for the topology and fiber paths of continuous fiber composites, Composites Part B: Engineering 183 (2020) 107681.
- [15] K. Bilisik, Multiaxis three-dimensional weaving for composites: a review, Textile Research Journal 82 (7) (2012) 725–743.
- [16] V. Hassani, An investigation of additive manufacturing technologies for development of end-use components: A case study, International Journal of Pressure Vessels and Piping 187 (2020) 104171.
- [17] S. Liu, S. Qin, Y. Jiang, P. Song, H. Wang, Lightweight high-performance carbon-polymer nanocomposites for electromagnetic interference shielding, Composites Part A, Applied Science and Manufacturing 145 (2021) 106376.
- [18] S. Zhu, Q. Zhou, M. Wang, J. Dale, Z. Qiang, Y. Fan, M. Zhu, C. Ye, Modulating electromagnetic interference shielding performance of ultra-lightweight composite

- foams through shape memory function, *Composites Part B: Engineering* 204 (2021) 108497.
- [19] S. Yuan, F. Shen, C.K. Chua, K. Zhou, Polymeric composites for powder-based additive manufacturing: Materials and applications, *Progress in Polymer Science* 91 (2019) 141–168.
- [20] N. Li, G. Link, T. Wang, V. Ramopoulos, D. Neumaier, J. Hofele, M. Walter, J. Jelonnek, Path-designed 3D printing for topological optimized continuous carbon fibre reinforced composite structures, *Composites Part B: Engineering* 182 (2020) 107612.
- [21] K. Sugiyama, R. Matsuzaki, A.V. Malakhov, A.N. Polilov, M. Ueda, A. Todoroki, Y. Hirano, 3D printing of optimized composites with variable fiber volume fraction and stiffness using continuous fiber, *Composites Science and Technology* 186 (2020) 107905.
- [22] G. Liu, Y. Xiong, L. Zhou, Additive manufacturing of continuous fiber reinforced polymer composites: Design opportunities and novel applications, *Composites Communications* 27 (2021) 100907.
- [23] R. Matsuzaki, M. Ueda, M. Namiki, T.-K. Jeong, H. Asahara, K. Horiguchi, T. Nakamura, A. Todoroki, Y. Hirano, Three-dimensional printing of continuous-fiber composites by in-nozzle impregnation, *Scientific reports* 6 (1) (2016) 1–7.
- [24] X. He, Y. Ding, Z. Lei, S. Welch, W. Zhang, M. Dunn, K. Yu, 3D printing of continuous fiber-reinforced thermoset composites, *Additive Manufacturing* 40 (2021) 101921.
- [25] X. He, Y. Ding, Z. Lei, S. Welch, W. Zhang, M. Dunn, K. Yu, 3D printing of continuous fiber-reinforced thermoset composites, *Additive Manufacturing* 40 (2021) 101921.
- [26] J. Jiang, Y. Ma, Path planning strategies to optimize accuracy, quality, build time and material use in additive manufacturing: a review, *Micromachines* 11 (7) (2020) 633.
- [27] Y. Xiong, S.-i. Park, S. Padmanathan, A.G. Dharmawan, S. Foong, D.W. Rosen, G. S. Soh, Process planning for adaptive contour parallel toolpath in additive manufacturing with variable bead width, *The International Journal of Advanced Manufacturing Technology* 105 (10) (2019) 4159–4170.
- [28] B. Aloyaydi, S. Sivasankaran, A. Mustafa, Investigation of infill-patterns on mechanical response of 3D printed poly-lactic-acid, *Polymer Testing* 87 (2020) 106557.
- [29] K. Sugiyama, R. Matsuzaki, A.V. Malakhov, A.N. Polilov, M. Ueda, A. Todoroki, Y. Hirano, 3D printing of optimized composites with variable fiber volume fraction and stiffness using continuous fiber, *Composites Science and Technology* 186 (2020) 107905.
- [30] A. L. Duigou, G. Chabaud, R. Matsuzaki, M. Castro, Tailoring the mechanical properties of 3D-printed continuous flax/PLA biocomposites by controlling the slicing parameters, *Composites Part B: Engineering* 203 (2020) 108474.
- [31] P. Pedersen, On optimal orientation of orthotropic materials, *Structural optimization* 1(2) (1989) 101–106.
- [32] P. Pedersen, On optimal orientation of orthotropic materials, *Structural optimization* 1(2) (1989) 101–106.
- [33] N. Li, G. Link, T. Wang, V. Ramopoulos, D. Neumaier, J. Hofele, M. Walter, J. Jelonnek, Path-designed 3D printing for topological optimized continuous carbon fibre reinforced composite structures, *Composites Part B: Engineering* 182 (2020) 107612.
- [34] T. Wang, N. Li, G. Link, J. Jelonnek, J. Fleischer, J. Dittus, D. Kupzik, Load-dependent path planning method for 3D printing of continuous fiber reinforced plastics, *Composites Part A: Applied Science and Manufacturing* 140 (2021) 106181.
- [35] R.R. Fernandes, N. van de Werken, P. Koirala, T. Yap, A.Y. Tamjani, M. Tehrani, Experimental investigation of additively manufactured continuous fiber reinforced composite parts with optimized topology and fiber paths, *Additive Manufacturing* 44 (2021) 102056.
- [36] D. Patel, D. Bielecki, R. Rai, G. Dargush, Improving connectivity and accelerating multiscale topology optimization using deep neural network techniques, *Structural and Multidisciplinary Optimization* 65(4) (2022) 1–19.
- [37] B. Brown, N.S. Hmeidat, X. Jia, J. Wilt, M. Roberts, B.G. Compton, N. Vermaak, Experimental investigations of the effectiveness of simultaneous topology/orientation optimization via SOMP and principal stress directions, *Materials & Design* 217 (2022) 110647.
- [38] A.A. Safonov, 3D topology optimization of continuous fiber-reinforced structures via natural evolution method, *Composite Structures* 215 (2019) 289–297.
- [39] H. Li, L. Gao, H. Li, X. Li, H. Tong, Full-scale topology optimization for fiber-reinforced structures with continuous fiber paths, *Computer Methods in Applied Mechanics and Engineering* 377 (2021) 113668.
- [40] J.P. Groen, O. Sigmund, Homogenization-based topology optimization for high-resolution manufacturable microstructures, *International Journal for Numerical Methods in Engineering* 113 (8) (2018) 1148–1163.
- [41] J.P. Groen, J. Wu, O. Sigmund, Engineering, Homogenization-based stiffness optimization and projection of 2D coated structures with orthotropic infill, *Computer Methods in Applied Mechanics and Engineering*, vol. 349, 2019, pp. 722–42.
- [42] S. Larsen, O. Sigmund, J. Groen, Optimal truss and frame design from projected homogenization-based topology optimization, *Structural and Multidisciplinary Optimization* 57 (4) (2018) 1461–1474.
- [43] D. Grund, M. Orlishausen, I. Taha, Determination of fiber volume fraction of carbon fiber-reinforced polymer using thermogravimetric methods, *Polymer Testing* 75 (2019) 358–366.
- [44] X. Tian, T. Liu, C. Yang, Q. Wang, D. Li, Interface and performance of 3D printed continuous carbon fiber reinforced PLA composites, *Composites Part A: Applied Science and Manufacturing* 88 (2016) 198–205.
- [45] K. Yamamoto, J.V.S. Luces, K. Shirasu, Y. Hoshikawa, T. Okabe, Y. Hirata, A novel single-stroke path planning algorithm for 3D printers using continuous carbon fiber reinforced thermoplastics, *Additive Manufacturing* 55 (2022) 102816.
- [46] J.M. Gere, B.J. Goodno, *Mechanics of materials*, Cengage learning2012.
- [47] R.C. Rumpf, J. Pazos, Synthesis of spatially variant lattices, *Optics express* 20 (14) (2012) 15263–15274.
- [48] X. Chen, G. Fang, W.-H. Liao, C.C. Wang, Field-based toolpath generation for 3D printing continuous fibre reinforced thermoplastic composites, *Additive Manufacturing* 49 (2022) 102470.
- [49] S.C. Chapra, R.P. Canale, *Numerical methods for engineers*, McGraw-hill, New York, 2011.
- [50] H.A. Abdulkarim, I.F. Alshammary, Comparison of algorithms for solving traveling salesman problem, *International Journal of Engineering and Advanced Technology* 4(6) (2015) 76–79.
- [51] V. Kesavan, R. Kamalakkannan, R. Sudhakarapandian, P. Sivakumar, Heuristic and meta-heuristic algorithms for solving medium and large scale sized cellular manufacturing system NP-hard problems: A comprehensive review, *Materials today: proceedings* 21 (2020) 66–72.
- [52] J.P. Trovão, P.G. Pereirinha, H.M. Jorge, C.H. Antunes, A multi-level energy management system for multi-source electric vehicles—An integrated rule-based meta-heuristic approach, *Applied Energy* 105 (2013) 304–318.
- [53] S. Kirkpatrick, C.D. Gelatt Jr., M.P. Vecchi, Optimization by simulated annealing, *science* 220 (4598) (1983) 671–680.
- [54] M.P. Bendsoe, N.J. Kikuchi, Engineering, Generating optimal topologies in structural design a homogenization method, *Computer Methods in Applied Mechanics and Engineering*, vol. 71(no. 2), 1988, pp. 197–224.
- [55] M.P. Bendsoe, Optimal shape design as a material distribution problem, *Structural Optimization*, vol 1 (1989).
- [56] K. Svanberg, The method of moving asymptotes—a new method for structural optimization, *Numerical Methods in Engineering*, vol. 24(no. 2), 2010, pp. 359–73.
- [57] K. Svanberg, A class of globally convergent optimization methods based on conservative convex separable approximations, *SIAM journal on optimization* 12 (2) (2002) 555–573.
- [59] S. Li, S. Yuan, J. Zhu, W. Zhang, Y. Tang, C. Wang, J. Li, Optimal and adaptive lattice design considering process-induced material anisotropy and geometric inaccuracy for additive manufacturing, *Structural and Multidisciplinary Optimization* 65 (1) (2022) 1–16.